Journal of Biomedical Optics

SPIEDigitalLibrary.org/jbo

Method for physiologic phenotype characterization at the single-cell level in non-interacting and interacting cells

Laimonas Kelbauskas
Shashanka P. Ashili
Jeff Houkal
Dean Smith
Aida Mohammadreza
Kristen B. Lee
Jessica Forrester
Ashok Kumar
Yasser H. Anis
Thomas G. Paulson
Cody A. Youngbull
Yanqing Tian
Mark R. Holl
Roger H. Johnson
Deirdre R. Meldrum

SPIE

Method for physiologic phenotype characterization at the single-cell level in non-interacting and interacting cells

Laimonas Kelbauskas,[a] Shashanka P. Ashili,[a] Jeff Houkal,[a] Dean Smith,[a] Aida Mohammadreza,[a] Kristen B. Lee,[a] Jessica Forrester,[a] Ashok Kumar,[a] Yasser H. Anis,[b] Thomas G. Paulson,[c] Cody A. Youngbull,[a] Yanqing Tian,[a] Mark R. Holl,[a] Roger H. Johnson,[a] and Deirdre R. Meldrum[a]
[a]Arizona State University, Biodesign Institute, Tempe, Arizona
[b]Cairo University, Faculty of Engineering, Giza, Egypt
[c]Fred Hutchinson Cancer Research Center, Seattle, Washington

Abstract. Intercellular heterogeneity is a key factor in a variety of core cellular processes including proliferation, stimulus response, carcinogenesis, and drug resistance. However, cell-to-cell variability studies at the single-cell level have been hampered by the lack of enabling experimental techniques. We present a measurement platform that features the capability to quantify oxygen consumption rates of individual, non-interacting and interacting cells under normoxic and hypoxic conditions. It is based on real-time concentration measurements of metabolites of interest by means of extracellular optical sensors in cell-isolating microwells of subnanoliter volume. We present the results of a series of measurements of oxygen consumption rates (OCRs) of individual non-interacting and interacting human epithelial cells. We measured the effects of cell-to-cell interactions by using the system's capability to isolate two and three cells in a single well. The major advantages of the approach are: 1. ratiometric, intensity-based characterization of the metabolic phenotype at the single-cell level, 2. minimal invasiveness due to the distant positioning of sensors, and 3. ability to study the effects of cell-cell interactions on cellular respiration rates.
© 2012 Society of Photo-Optical Instrumentation Engineers (SPIE). [DOI: 10.1117/1.JBO.17.3.037008]

Keywords: single-cell; respiration; heterogeneity; optical sensing; microfluidics; microfabrication; cell-cell interactions.

Paper 11577P received Oct. 5, 2011; revised manuscript received Jan. 26, 2012; accepted for publication Jan. 27, 2012; published online Apr. 5, 2012.

1 Introduction

Cell-to-cell heterogeneity is a major factor in many vital cell processes including differentiation, proliferation, survival, stress response, and carcinogenesis. It can be caused by genetic and/or nongenetic variations in the cell. Although genetic heterogeneity results from alterations in the genomic DNA sequence, nongenetic intercellular heterogeneity is caused by intrinsic (e.g., differences in gene expression) and/or extrinsic (e.g., microenvironmental factors) noise in gene transcription machinery, which results in differential gene expression levels that can lead to phenotypic alterations in a cell.[1–3] Under stress conditions, this phenotypic heterogeneity can, in turn, lead to changes in a cell's homeostasis, survival, or death because of a transiently high or low abundance of relevant proteins, imparting to the cell a selective advantage over other cells under given conditions.[4] Studies of intercellular variability are therefore critical as they can help reveal novel details as to why and how cells alter their phenotypes from benign to malignant. In addition to providing deeper insight into fundamental questions of cell biology, studies on cell population heterogeneity bear the potential of opening new ways for prevention and more effective treatment of cancer and other diseases with high morbidity and mortality. The most direct way to address intercellular heterogeneity is to perform studies at the single-cell level. Information with single-cell resolution, such as how the phenotype of one individual cell differs from another and what implication these differences may have in the context of cell population, is crucial to understanding the behavior of complex multicellular organisms.

Most experimental methodologies for cellular phenotype characterization provide ensemble-averaged data based on the analysis of bulk samples comprising 10^5 to 10^7 cells. Studies with individual cells pose several challenges to existing technologies, including the requirement for high-detection sensitivity and specificity.[5] Because of the small volumes (~500 fL) and the number of biomolecules in a single mammalian cell, alterations in the physiologic cell state need to be measured with ultra-high sensitivity, far exceeding that of bulk cell experiments. In recent years, the field of single-cell biology research has benefited from significant advances and technological developments that permit the genome,[6,7] transcriptome,[8,9] and proteome[9,10] to be studied at an unprecedented level of detail. However, these techniques are disruptive end-point analyses that provide only a snap-shot in time of a cell's state. For a deeper understanding of the changes a cell undergoes in dynamic response to stimuli and stress, studies of cellular-response mechanisms in real time are necessary.

One vital cellular process is energy production by oxidative phosphorylation. Oxidative phosphorylation requires molecular oxygen as an electron acceptor at the end of the electron transport chain, thus resulting in characteristic oxygen consumption rates in aerobic organisms. Because almost every molecular

Address all correspondence to: Laimonas Kelbauskas, Biodesign Institute, Arizona State University, Tempe, Arizona. Tel: (480) 965 3128; Fax: (480) 727 6588; E-mail: lkelbaus@asu.edu.

0091-3286/2012/$25.00 © 2012 SPIE

mechanism inside the cell depends on the energy stored in high-energy bonds in the form of ATP, changes in the physiologic state of a cell will be reflected in alterations in energy demand.[11–14] Therefore, changes in oxygen consumption can serve as a sensitive indicator for alterations in the physiologic state of the cell.

Several different approaches have been developed for measuring oxygen in single live cells. Geissbuehler et al.[15] used the quenching of the triplet state of a fluorophore by oxygen to quantify changes in intracellular oxygen concentration.[15] Other approaches employed direct detection of singlet oxygen phosphorescence in single cells.[16,17] Although providing a tool for intracellular oxygen concentration measurements, these methods do not enable the determination of oxygen consumption kinetics. The available experimental approaches for oxygen consumption measurements in individual cells can be divided into two groups: one set of techniques is based on microprobes,[18–22] whereas the second involves the isolation of individual cells in microwells.[23–26] Although microprobe methods provide a robust and sensitive tool for oxygen flux measurements at the single-cell level, they suffer from several limitations, including low throughput (one cell at a time) and the inability to separate potential contributions from adjacent cells in high-density cultures.

Optical sensors offer several advantages over electrochemical probes, as they are relatively simple to produce, feature fast response times, and most importantly, consume minimal oxygen. In addition, optical sensing offers the capability of multiplexing by using spectrally or spatially separated microsensors. Multiplexing electrochemical probes would require operating multiple microelectrodes within small volumes in the vicinity of the cell to be interrogated. Submicrometer-sized, ratiometric, fiber-optic oxygen sensors have excellent sensitivity, reversibility, and stability characteristics, and have been proposed for measurements of intra and extra-cellular oxygen concentration in single-cells.[27]

A different approach for measuring oxygen consumption rates of individual cells has been developed by our group and is based on the measurements of oxygen fluxes in isolated hermetically sealed microwells containing single cells.[23–26] In contrast to microprobe-based oxygen consumption measurements, methods based on isolation of individual cells in microwells offer at least one order of magnitude higher throughput and true single-cell measurement capability. Enclosing individual cells in hermetically sealed chambers provides a unique possibility to measure isolated oxygen consumption with true single-cell resolution. These methods rely on measurements of the luminescence lifetime of an optical sensor as a function of oxygen concentration in a sealed chamber containing a single cell. However, although offering adequate dynamic range and sensitivity, lifetime-based techniques require fairly complex and expensive excitation sources and detection electronics. Owing to the relatively long luminescence lifetimes (microseconds) of the oxygen sensors (see Ref. 28 and references therein), technical requirements for high-speed electronics on the excitation and detection components are somewhat relaxed.[28] However, the slow, microsecond-long emission lifetimes of metallo-porphyrin complexes or ruthenium-based oxygen sensors represent the exception among optical sensors. Most optical sensors designed for other biological analytes of interest, including Ca^{2+}, Zn^{2+}, K^{+}, and Na^{+}, exhibit excitation decay times in the nanosecond range. As a result, using these sensors for emission lifetime-based measurements for the corresponding analytes would require either subnanosecond pulsed (for time-domain lifetime measurements), or multiple high-speed modulated (for frequency-domain lifetime measurements), excitation sources replete with complex timing circuitry, and data acquisition and analysis software.

Another, nontrivial aspect of perhaps equal importance in isolation-based methods is sample preparation. Creating cultures of single cells in the required arrangement, i.e., individual cells placed at particular distances inside microfabricated features for the production of sealed chambers, represents a challenge in itself. The reported methods[23–26] use random cell seeding, where the bottom part (wells) of the microwells are populated with cells by randomly distributing cells suspended in media over an array of wells. Although the approach is simple and produces satisfactory results, its major limitation is the low efficiency of populating the wells with single cells. Even after careful optimization of cell concentrations, it is impossible to precisely control the number of cells per well, which generally results in a Poisson distribution of the number of cells populating individual wells. For single-cell analysis, random seeding produces a bottleneck in the overall experimental flow, lowering the throughput, as only a fraction of wells will contain single cells. More importantly, random seeding does not allow targeted selection of cells of interest, e.g., based on fluorescence staining, to be loaded into the wells. Another shortcoming of these methods is the immediate vicinity of the sensor to the cells, which may adversely influence normal cell function because of photochemical activity of the sensor, including reactive oxygen species and singlet oxygen production.

To address the limitations of current technologies, we developed an improved, efficient, integrated platform for studies of intercellular oxygen consumption heterogeneity at the single-cell level. The system is based on microfabricated devices and extracellular optical sensors and is potentially expandable to multiparameter metabolic phenotype characterization in individual cells. The approach features a highly efficient, aspiration-based cell loading technique that achieves rapid, minimally invasive loading of single cells of different types into microwells. The cell loading method facilitates image-based selection of cells of interest based on morphologic features or specific fluorescence probes in or on the cell. To address any potential issues involving sensor proximity to the cell, the extracellular sensors are separated from the cells by approximately 30 μm. In contrast to the previous techniques, we quantify oxygen concentration based on a ratiometric measurement of the sensor emission intensities, which is a function of oxygen concentration within the sealed microwell containing the cell.

Compared with the previous cell isolation-based techniques, the approach presented in this paper offers the following advantages: 1. relatively simple intensity-based ratiometric measurements that can easily be integrated on existing commercial imaging systems; 2. ability to select and load desired numbers of individual cells of interest for intercellular interaction studies; 3. significantly decreased sensor phototoxicity and biocompatibility effects because of sensor positioning at a distance from the cell; and 4. higher overall throughput. We present system characterization data and experimental results of single-cell respiration measurements on isolated or interacting, cultured, human epithelial cells. Future applications, including the developments for multiparameter sensing and extensions of the approach are discussed.

2 Materials and Methods

2.1 *Microwell Design*

Our approach is based on enclosing single cells in hermetically sealed fused silica (glass) microwells of about 140 pL volume containing extracellular optical sensor material embedded in a polymer matrix. Ratiometric measurements of sensor emission intensity changes in response to oxygen concentration alterations were conducted using this sealed microwell and optical sensing phenotype characterization apparatus. In the current implementation 3×3 arrays of symmetrically arranged microwells (50 μm ID and 20 μm deep) and matching lids [80 μm ID and 20 μm deep; Fig. 1(a), 1(b)] were used. Lids and microwells were fabricated in fused silica substrates using wet-etch lithography.[29] The hermetic seal was produced by placing lipped lids containing the extracellular oxygen sensor on top of the microwells and applying pressure to the lid array [Fig. 1(c), 1(d)]. A layer of compliant material was placed between the piston and the lid substrate to ensure equal force distribution across the lids.

2.2 *Cell Culture*

For this study, we used two immortalized human esophageal epithelial cell lines, CP-A and CP-C, derived from patients with Barrett's esophagus without dysplasia and with dysplasia, respectively.[30] Cells were cultured in T75 tissue-culture flasks (Corning, Corning, NY) to approximately 80% confluence, at which time they were trypsinized, centrifuged at 900 rpm for 3 min, and resuspended in 2 mL of cell growth medium.

The CP-A and CP-C cells were grown at 37°C, under 5% CO_2 atmosphere in cell culture flasks using GIBCO® Keratinocyte SFM cell growth medium (Invitrogen, Carlsbad, CA), supplemented with hEGF (Peprotech, Rocky Hill, NJ) at 2.5 μg/500 mL, bovine pituitary extract (BPE) at 25 mg/500 mL and penicillin/streptomycin solution (Invitrogen) at 100 units/100 μg/mL. Prior to loading, cells were detached from the flask bottom using 0.05% trypsin-ethylenediaminetetraacetic acid (EDTA) solution and transferred to a Petri dish.

2.3 *Cell Loading into Microwells*

Individual cells were loaded using a custom microfluidic platform[31] optimized to enable aspirating and dispensing one or multiple cells into each microwell. The cell loader is built around a custom designed high-precision diaphragm micropump that allows for subnanoliter volumes to be aspirated and dispensed in a highly controlled manner.[32] Single cells were aspirated and dispensed using a glass micropipette with a tip of 40 μm inner diameter attached to the pump. To accomplish the loading of a single cell, the cell of interest was brought into the center of the field of view of the microscope objective. Then, the tip of the micropipette that was attached to the micropump was lowered

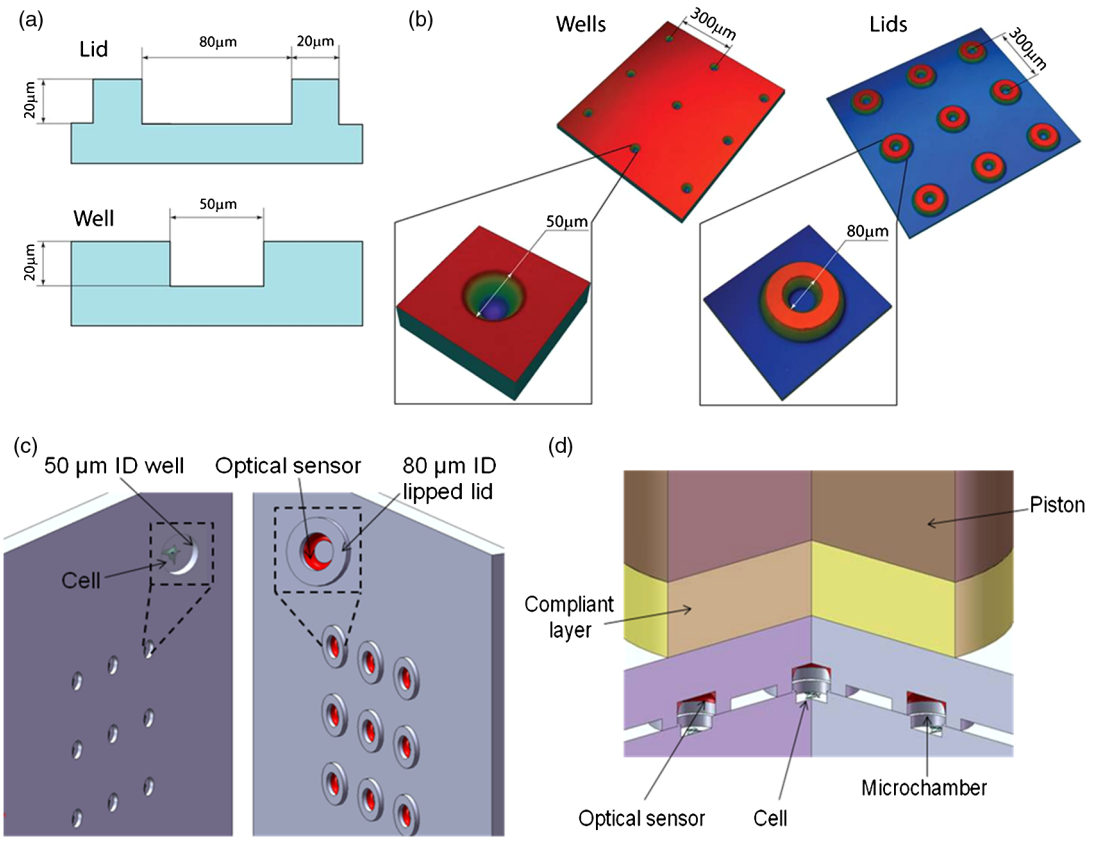

Fig. 1 Microwell array design and characterization. (a) Design of the upper (lid) and lower (well) parts of the microwells used in this study. Different designs were tested to optimize seal integrity for high oxygen sensitivity. Dimensions were chosen to provide uncomplicated cell loading into wells. (b) Topographic images of wells and lids obtained utilizing noncontact optical profilometry. 3×3 arrays of wells and lids with 300-μm center-to-center spacing were fabricated on fused silica wafers using hydrofluoric acid (HF) deep wet etch lithography. Well and lid sidewalls show isotropic etch profile (insets). Average surface roughness was ~16 nm for 20-μm etch depth. Overall process yield and repeatability was >90%.[29] (c) 3×3 array of microwells and lids microfabricated in fused silica substrate, and (d) hermetically sealed microwells with a total volume of 140 pL.

and positioned within 40 to 70 μm from the cell, and then the cell was aspirated into the micropipette by the micropump. Once the aspiration step was complete, the micropipette tip was raised and aligned with a second Petri dish containing the microwell substrate using a motorized microscope stage.

After trypsinization, the cells were loaded into microwells immediately to prevent cells from adhering to the bottom of the Petri dish. Glass substrates containing 3×3 arrays of microwells were glued to the bottom of a Petri dish with a precut hole of a slightly smaller diameter than the substrate using medical-grade epoxy glue (K45-S-14ML, Chemical Concepts, Huntingdon Valley, PA). The Petri dish containing the microwell array was placed on the cell loader platform adjacent to the Petri dish containing suspended cells. For single-cell experiments, loading was performed by aspirating one or several cells into the micropipette at a time. For the experiments with 2 or 3 cells per well, individual cells were aspirated and loaded in the microwells one at a time. This was necessitated by the need for higher precision in the fluid flow control required to prevent an already loaded cell from being ejected from a well while loading the next one. The dispensing step was conducted using a computer-controlled vision-feedback algorithm that facilitated the release of one cell at a time from the micropipette tip; this required 5 to 8 min to load a 3×3 array of microwells with 1 cell per well. Loading 2 or 3 cells per well in a 3×3 array required 15 to 25 min.

After loading cells into the microwells, the arrays were incubated for 16 to 24 h under normal physiologic conditions to allow for cell adhesion and recovery from potential stress caused by manipulation [Fig. 2(a)]. No lid was placed on top of the wells during incubation to ensure cell access to nutrients and oxygen. We assessed cell viability after cell loading and incubation using the CalceinAM/Sytox Orange live/dead assay (Invitrogen, Carlsbad, CA). We found that $> 99\%$ of cells loaded in microwells showed enzymatic activity. Five to 10% of loaded cells divided in the microwells during the incubation time, which suggests excellent cell health and near-normal function after confinement in microwells. We account for these microwells by using transmission bright-field imaging to determine the number of cells in each microwell prior to experiments. Wells containing cells that underwent division during the incubation time are not included in the data analysis.

2.3.1 *Cell loading software overview and description*

The cell loading software was implemented as a LabVIEW (National Instruments, Austin, TX) program used to automate the cell loading process, i.e., the process of selecting cells from a source Petri dish and transferring them to a selected destination microwell array for use in OCR experiments. Although the main LabVIEW program provides automation for cell loading-specific tasks, the system software uses generic laboratory automation code libraries to provide access to and automation of the system components.

The user interface is a LabVIEW program that allows the user to select from a variety of automation tasks required to accomplish the cell loading process. These tasks include: automated positioning of the Petri dish over the objective lens and under the transfer pipette, automated positioning of the selected microwell array over the objective and under the transfer pipette, raising and lowering of the pipette, and control of the picopump (Fig. 3).

2.4 *Sensor Deposition and Characterization*

To quantify oxygen concentration in the microvolume surrounding a cell we used a self-referencing, ratiometric measurement of sensor emission intensity. The main advantage of this approach is that the signal is independent of deposited sensor volume.

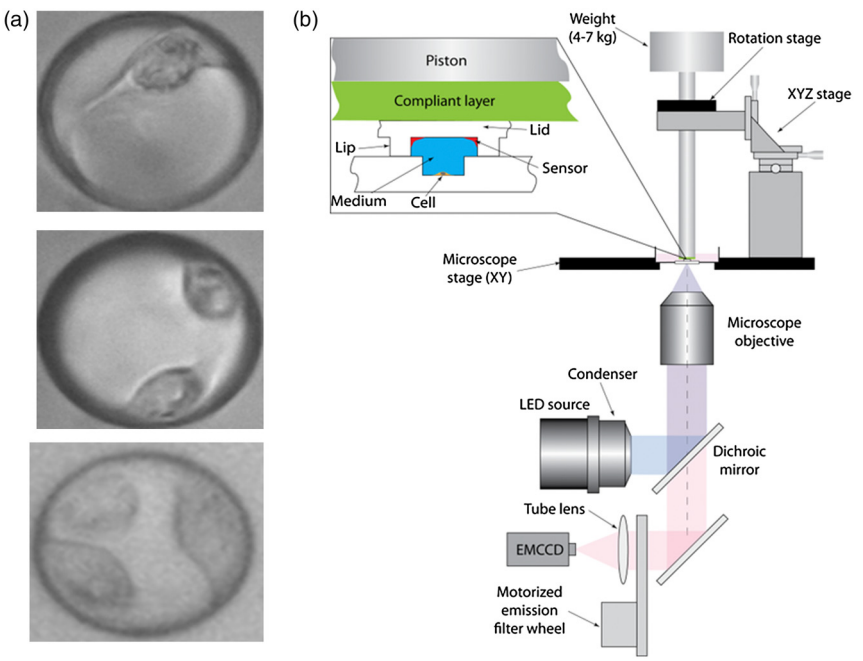

Fig. 2 Experimental single-cell respirometry platform. (a) Micrographs of microwells with 50-μm ID containing one (top), two (middle), and three (bottom) CP-A cells incubated 22 h after cell loading; and (b) single-cell OCR experimental setup. Prior to producing gas impermeable seal, lid and microwell were aligned using motorized rotation stage and manual XYZ stage mounted on the microscope XY stage. Inset: close-up view of microwell produced by placing array of lids over microwells containing single cells.

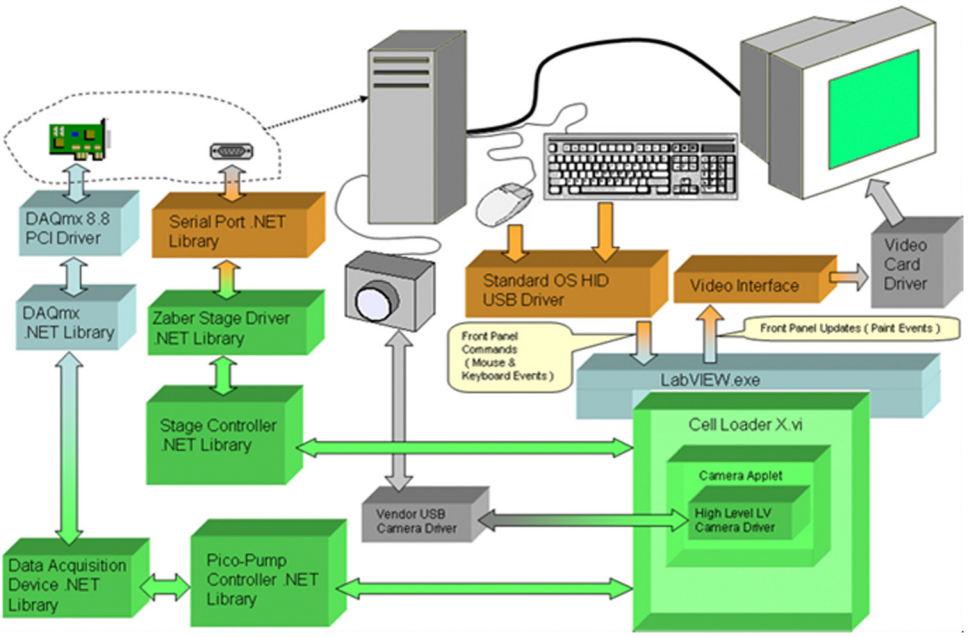

Fig. 3 Cell loading software architecture overview.

We used platinum porphyrin derivative, Pt(II) Octaethylporphine (PtOEP, Frontier Scientific, Logan, UT) as the oxygen sensor and silicon octaethylporphine (SiOEP, Frontier Scientific) as the reference luminophore. For deposition in the microwells we used 1 mg PtOEP (O_2 sensor) and 1 mg SiOEP dissolved in 1 g of monomer ethyoxylated-(3)-trimethylolpropane triacrylate (SR454, Sartomer, Exton, PA) solution containing 10 mg azobisisobutyronitrile (AIBN, Sigma-Aldrich, St. Louis, MO). AIBN was used as a thermal initiator of free radical polymerization of SR454. The mixture was sonicated until a homogenous solution was obtained and then stored at 4 °C until used.

The sensor was deposited in lids using a noncontact piezoelectric liquid dispensing robot (Rainmaker au301, Aurigin Technology Inc., Phoenix, AZ). We deposited 100 to 200 pL of sensor material in each microwell lid. The deposition step took approximately 200 µs for each lid (Fig. 4). The fused silica (interior lid) surface receiving the sensor material droplet was functionalized with a companion moiety designed to covalently bind to the SR454 polymer matrix. Prior to sensor deposition the lid surface was cleaned, plasma-treated, and functionalized with trimethylsilylpropyl acrylate (TMSPA) by vapor deposition. TMSPA binds to the hydroxyl radicals on the fused silica surface generated by the plasma treatment. SR454 monomer containing

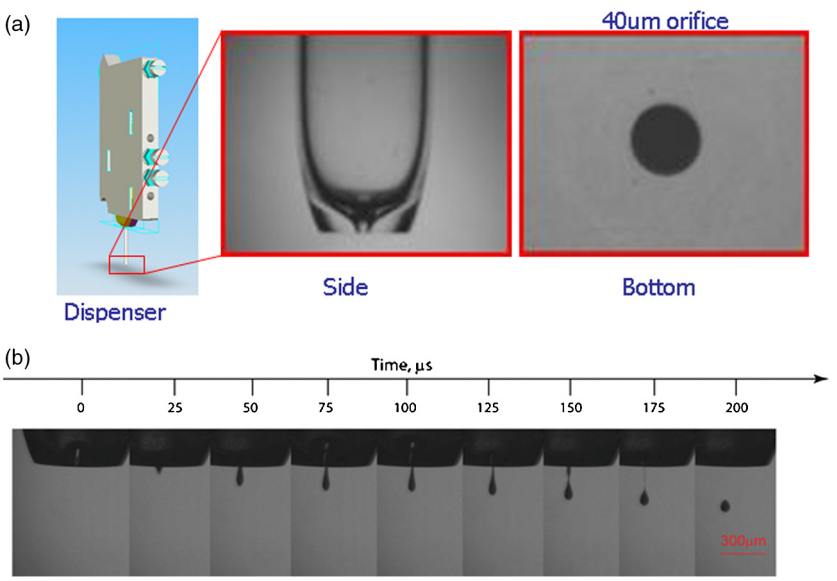

Fig. 4 Sensor deposition. (a) Schematic representation of piezoelectric sensor dispenser head (left); micrograph of glass capillary with nozzle (middle); micrograph of 40-µm nozzle orifice (right). (b) Stroboscopic time series of sensor droplet deposition. Sensor material is dissolved in SR454 monomer. Time series shows formation of ~100 pL ($D \sim 57$ µm) droplet of SR454 by focusing acoustic wave produced by piezoelectric element at convergent orifice of capillary. Dispensing of droplet takes 200 µs.

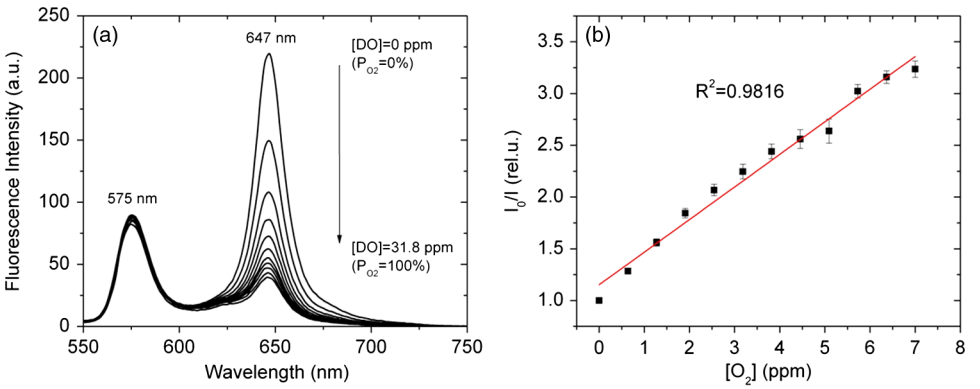

Fig. 5 Ratiometric oxygen sensor calibration. (a) Emission spectra and intensity response of combined SiOEP and PtOEP sensor in SR454 thin-film matrix at various oxygen concentrations. Reference dye SiOEP has emission maximum at 575 nm. Emission intensity of SiOEP does not change with O_2. PtOEP emission intensity, with maximum at 647 nm, exhibits strong inverse dependence on O_2. (b) Calibration of PtOEP/SiOEP sensor after deposition in lids. Different O_2 concentrations were obtained utilizing a high-precision gas mixing manifold. Solid line represents a Stern-Volmer fit to the calibration data.

the sensor binds covalently to the acrylate moiety of the surface-bound TMSPA during thermal polymerization. After deposition the substrates were placed into a vacuum drying oven (DX400, Yamato, Santa Clara, CA) and thermally cured for 3 h at 80°C under nitrogen atmosphere (70 mm Hg/0.01 MPa).

Although the PtOEP phosphorescence signal depends strongly on oxygen concentration (O_2) in the surrounding medium, the SiOEP fluorescence intensity remains constant over a wide range of O_2 [Fig. 5(a)]. The sensor response to changes in O_2 was calibrated using reference solutions containing known concentrations of dissolved oxygen. The reference aqueous solutions were prepared by purging water or cell culture media with N_2 + O_2 gas mixtures of the desired oxygen concentrations obtained using a computer controlled gas manifold (Alicat Scientific, Tucson, AZ). The calibration data were used for oxygen concentration determination in the OCR measurements. Fig. 5(b) shows calibration of the sensor in lids submersed in cell media. The measured data points were fit with the Stern-Volmer equation to create a continuous calibration curve. The goodness of fit supports the assertion that sensor emission intensity is governed by diffusion-limited dynamic quenching by oxygen.

2.5 *Experimental Setup*

The OCR measurements were performed on a custom experimental platform built around an inverted microscope [Eclipse TE2000, Nikon, Melville, NY; Fig. 2(b)]. All experiments were performed at 37°C, controlled by means of an environmental chamber enclosing the microscope. The sensor was excited using a narrow-band LED with an emission maximum of 396 nm (Lumibright, Innovations in Optics, Woburn, MA) coupled to the epi-illumination port of the microscope. A diffuser was placed in front of the LED to produce uniform illumination of the field of view. The sensor was excited and emission photons were collected utilizing a 10×, 0.45 NA Plan Apochromat objective lens (Nikon) and a dichroic mirror (440 dclp, Chroma Corp., Bellows Falls, VT) mounted in the filter turret of the microscope. The emission signal was passed through one of two band-pass filters (BP595/70 and BP650/50, Omega Optical, Brattleboro, VT) for SiOEP and PtOEP emissions, respectively. These filters were mounted on a motorized filter wheel rotating in an infinity plane outside the microscope. Sensor emission images were collected using a cooled, electron multiplying, charge-coupled device camera (Cascade II 512, Photometrics, Tucson, AZ). The LED was operated in a pulsed mode synchronized to the camera exposure time to ensure that sensor excitation occurred only during image acquisition. Sensor data was captured every 5 sec with an exposure time of 20 ms per spectral channel. Alignment of well and lid arrays and the production of an air-tight seal between them, were accomplished using a high precision XYZ translation stage and a motorized rotation stage mounted on the microscope stage (Fig. 6).

Sensor intensity data was extracted from the images by defining threshold-based, annular or circular regions of interest (ROIs) encompassing each sensor's area and calculating the average intensity value within each ROI. The average intensity values in both spectral detection channels were calculated using the following equation:

$$I_{\text{ave}} = \frac{\sum_{k=1}^{N} I_k}{N}, \tag{1}$$

where N is the number of pixels in a ROI and I_k is the intensity of k'th pixel.

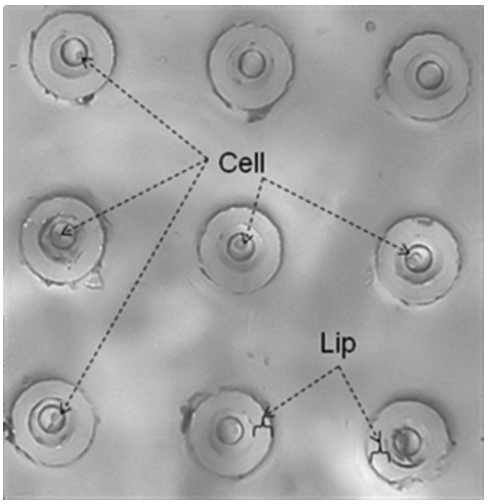

Fig. 6 Bright-field micrograph of 3 × 3 array of hermetically sealed microwells containing single cells.

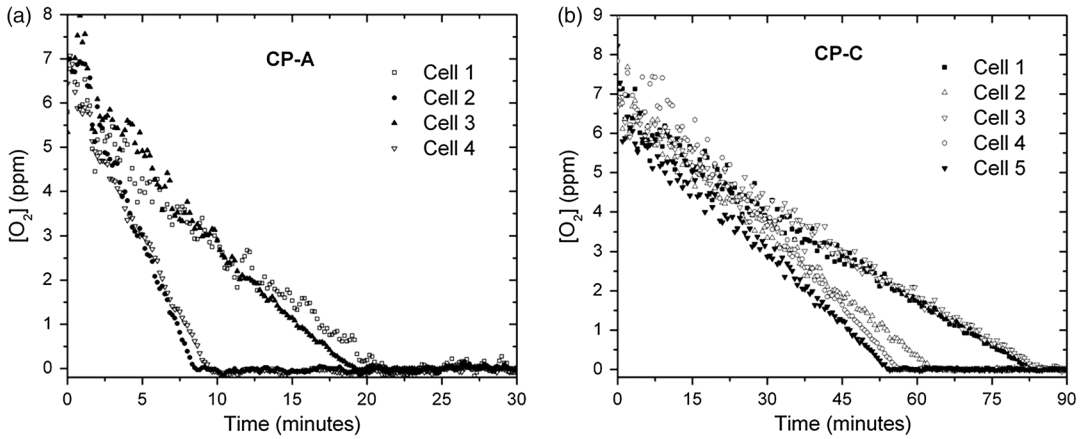

Fig. 7 Comparison of single-cell OCR results obtained with two different cell lines. All cells were treated identically and incubated for 16 to 24 h prior to OCR measurement. (a) OCR curves obtained with single cells of metaplastic human esophageal epithelial cell line CP-A. (b) OCR time courses of slowly respiring individual cells of dysplastic human esophageal epithelial cell line CP-C. All cells exhibit linear OCR kinetics. Significant cell-to-cell variations in OCR are demonstrated. Signal-to-noise ratio observed in OCR traces increases as O_2 decreases because of stronger sensor emission intensity at low O_2. Data in all panels smoothed with sliding five-point average filter.

2.6 *Data Analysis*

Statistical analyses of the data and data fitting procedures were performed using OriginPro software (v. 8, OriginLab, Northampton, MA). Data analysis software was written using LabView 8.6 (National Instruments, Austin, TX). We note that although all oxygen consumption data were analyzed after the experiments, the same type of analysis can easily be performed in real-time as well. We are currently modifying the software code to accomplish this task.

3 Results and Discussion

Oxygen concentration in the microwells was determined every 5 s as described in "Materials and Methods". The sensor intensity values were converted to oxygen concentration using calibration data obtained from the same sensor-containing lid prior to experiments on isolated, live cells. Rather than absolute PtOEP intensity values, we used ratiometric calibration and conversion to oxygen concentration based on the ratio of PtOEP and SiOEP emission intensities. Because of cell respiration, after the lids were sealed, the O_2 in the microwells fell monotonically from ambient levels (7 ppm; 21%) to below the limit of detection (LOD). We define the LOD as the change in O_2 needed to produce a change in sensor emission intensity equal to three times the standard deviation of a blank sample (0% O_2) signal. We determined the LOD of our system to be 168 ppb, comparable with those reported in other studies.[27] As the oxygen concentration in the microwell decreases, the signal-to-noise ratio (SNR) of the sensor system increases with emission intensity. The average SNR at the beginning and the end of the experiment are 4 (ambient O_2) and 8 (low O_2), respectively. This increase was caused by the increase in sensor emission intensity owing to decreased quenching of the triplet state of PtOEP by molecular oxygen.

3.1 *Respirometry of Individual, Non-Interacting Cells*

To evaluate system performance characteristics we measured OCRs of single cells from two different human epithelial cell lines, CP-A and CP-C, which were derived from patients having diagnoses of Barrett's esophagus without dysplasia and with dysplasia, respectively.[30] Characteristic oxygen consumption curves for the two cell lines are presented in Fig. 7. We observed significant cell-to-cell differences in OCRs within each cell line and between the cell lines, with variations exceeding six-fold within a single cell line. Within a single experiment accommodating nine cells of a given cell line, we see marked OCR variations in all cell types. For example, the time needed to reach a 0% O_2 in the microwell varies by about a factor of two for the CP-A cells [Fig. 7(a)]. Figure 7(b) shows responses of a subset of the CP-C cells that exhibited slow respiration kinetics. A significant portion of CP-C cells showed faster respiration kinetics, similar to those shown in Fig. 7(a) for CP-A cells. The fraction of slower-respiring CP-C cells [Fig. 7(b)] seem to exhibit less variability in OCR, as the times to approach 0% O_2 vary only by factor of approximately 1.5. This implies that faster-respiring, more metabolically active cells may differ more from each other than less active, slow-metabolizing cells of the same type. The observed OCR heterogeneity within a cell type may be partially attributed to the use of non-synchronized cells in these experiments. Each cell's phase in the cell cycle probably contributed to the variability in OCR in addition to intrinsic intercellular heterogeneity.

All oxygen consumption kinetics exhibited linear behavior with a constant OCR in the oxygen concentration range between 7 and ~0.2 ppm. Below 0.2 to 0.1 ppm, the OCR exhibits a non-linear dependence on O_2 concentration (Fig. 8). In this study, we do not focus on oxygen consumption kinetics in this low range of O_2. Because it is thought provoking, other studies are underway to address this finding in more detail. We exclude the possibility that the observed nonlinearity in the respiration curve in this O_2 range is caused by changes in the sensor response as oxygen concentration decreases. The sensor calibration demonstrated that sensor emission intensity changes caused by differences in the amount of oxygen can be well described by the Stern-Volmer law, and do not exhibit any significant deviations as the oxygen concentration changes. Therefore, we attribute the observed nonlinear behavior at low O_2 to real alterations in cell OCRs.

To calculate OCR values for each of the studied cells we applied a linear fit to the oxygen consumption time course data above 0.2 ppm (Fig. 9). The chosen linear function

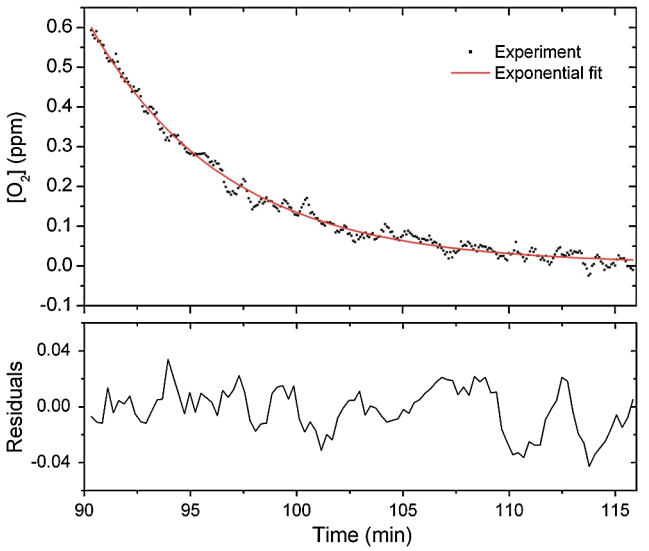

Fig. 8 Oxygen consumption in CP-C cells under severe hypoxia. Shows zoomed-in region of low O_2 of the respiration time course of cell 5 in Fig. 7(b). At O_2 levels <0.5 ppm respiration behavior is well fit with exponential relation (solid curve).

might not be the most accurate: other, more complex models may exist that describe the observed behavior more appropriately. However, the SNR intrinsic to the current realization of the method limits the ability to resolve more details. The linear fit was chosen to provide a means for quantitative analysis and comparisons among cells within and between cell lines. We calculated the OCR values using the slopes of the linear regression fit and converting the values into oxygen concentration using the following equation:

$$\mathrm{OCR} = \frac{Vb}{m}, \tag{2}$$

where V is the total volume of the microwell, b is the slope of linear regression model, and m is the molecular weight of O_2.

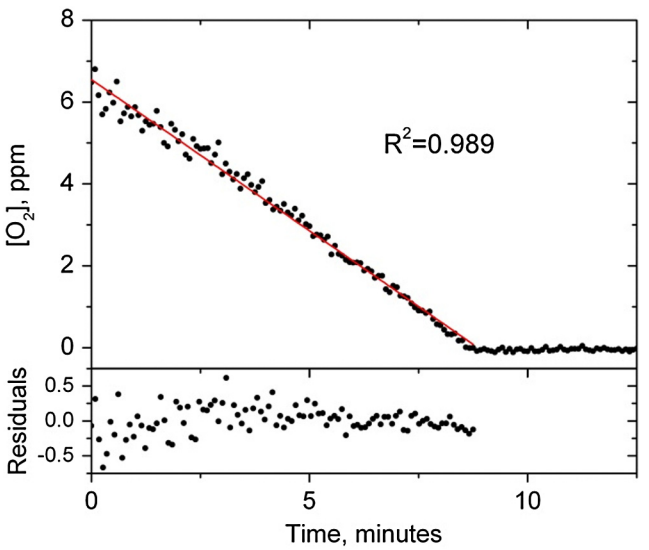

Fig. 9 OCR data analysis. Linear regression fit (solid line) to experimental data. Lower panel shows residuals of fit.

OCR distribution histograms of CP-A and CP-C cells are presented in Fig. 10(a). A two-sample t test showed that at the $P = 0.05$ level the difference of the population means is not significantly different. However, a comparison of the two cell lines shows that there are differences in the high OCR regime between 2 and 6 fmol/(min · cell). Even though the majority of the CP-A and CP-C cells exhibit OCR

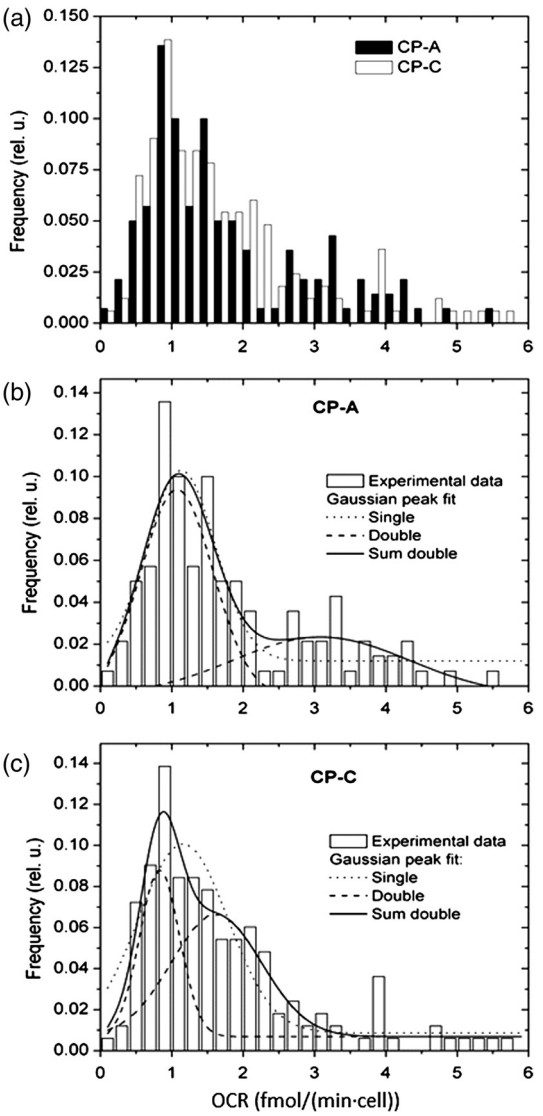

Fig. 10 Summary of single-cell oxygen consumption rate (OCR) results. (a) Distribution of single-cell OCRs in CP-A and CP-C cells. Significant cell-to-cell variations in OCR within each cell line are observed. Broad distributions may result from cells being in different cell cycle phases and/or intrinsic cell-to-cell heterogeneity. Means of two distributions are not significantly different at $P = 0.05$, but the presence of subpopulation of CP-A cells (but not CP-C cells) with OCRs between 2 and 5 fmol/(min · cell) suggests metabolic differences between cell lines. (b) Single (blue curve) and double (green curves, red curve—sum) Gaussian fits were applied to CP-A (b) and CP-C (c) OCR distributions. Fits show at least two subpopulations of cells within each cell type. Fit results are summarized in Table 1. The differences in the OCR distribution shapes between CP-A and CP-C cells demonstrate the capability of the method to distinguish and characterize groups of cells by resolving intercellular differences in OCR in individual cells, where conventional, bulk sample-based approaches would fail to do so.

values centered around the population average (Table 1), a fraction of cells respires at rates significantly higher (up to ~600%) than this average. This demonstrates the capability of the technique to identify outliers in a population of cells in terms of their respiration rate.

To better characterize the differences in OCR distribution between the CP-A and CP-C cells, we performed Gaussian fits on the OCR histograms. Although it may not represent the best fit to the data, the Gaussian model was chosen to reveal quantitative differences between the two types of cells. We applied two Gaussian peak functions to fit the OCR histograms of both cell types [Table 1; Fig. 10(b), 10(c)]. The fits show that at least two subpopulations exist among the CP-A and CP-C cells in terms of their respiration rates. CP-A cells exhibit one "slow" fraction with OCR values centered at 1.07 ± 0.08 fmol/(min · cell) and a second, "fast" subpopulation with an OCR of 3.1 ± 0.6 fmol/(min · cell); (the absolute error values indicated here and below represent the fit error). The fractional contributions of the slow and fast subpopulations are 59% and 41%, respectively. Use of the terms "fast" and "slow" in this context are relative and meant to reflect the comparative nature of the data analysis. The CP-C cells show less distinct differences in the two subpopulations compared with CP-A. The slow fraction of CP-C cells has an average OCR of 0.83 ± 0.04 fmol/(min · cell) with a fractional contribution of 38%, whereas the fast fraction is centered at 1.63 ± 0.27 fmol/(min · cell) with a fractional contribution of 62% of cells.

The observed OCR heterogeneity and the differences in single-cell OCRs between cell types confirm the need for single-cell studies. Ensemble-averaged OCR studies conducted on samples of hundreds of thousands or millions of cells, or mitochondria isolated from similar numbers of cells, revealed a substantially linear oxygen consumption profile for O_2 in the range from 7 to 0.1 ppm, and a hyperbolic profile at oxygen levels less than 0.1 ppm.[33–35] These findings are in accord with the temporal characteristics of the average OCR behavior observed in this study. Because different cell types were used in the previous studies and this work, it seems that the observed common features of the OC kinetics are cell type-independent. Obviously, more studies on different cell types need to be conducted to confirm (or refute) this finding. Differences between OCR values observed at the single-cell level in this study and the bulk cell samples of previous reports may have two different origins. One stems simply from the fact that the cell types used in the previous and this study are different, thus making it probable that OCR values can differ because of differences in basal respiration rates. The second source of difference can be the averaging of millions of unsynchronized responses of individual cells inherent to bulk experiments. As evident from the OCR data presented in this study [Figs. 7 and 10(a)], unsynchronized individual cells exhibit significant variations in oxygen consumption rate. Even so, the average OCR values for CP-A and CP-C cells were found not to be statistically different. In terms of their OCRs, at least two subpopulations were found in the CP-A and CP-C cell groups. Thus, strong evidence is presented, which supports the assertion that averaging OCR data from $\sim 10^5$ to 10^7 cells results in obscuring details of respiration kinetics and the cells' physiologic responses to oxygen concentrations. Details that may be obscured include the substantial cell-to-cell differences in OCR and the existence of subpopulations of cells with a differing metabolism.

Table 1 Summary of OCR results from CP-A and CP-C cell lines.

Cell type	OCR_{ave}[a]	S.E.M.[b]	N[c]	Gaussian fits			
				Single, R^2_{adj}[d]	Double, R^2_{adj}	Subpopulation OCR_{ave} (fmol/min · cell)	
						Slow (FC)[e]	Fast (FC)
CP-A	2.54	0.27	140	0.74	0.83	1.70 ± 0.08[f] (59%)	3.1 ± 0.6[f] (41%)
CP-C	1.99	0.14	166	0.79	0.92	0.83 ± 0.04[f] (38%)	1.6 ± 0.3[f] (62%)

[a]Average OCR value calculated using all studied cells of the corresponding cell line.
[b]Standard Error of Mean.
[c]Number of single-cells studied.
[d]Adjusted coefficient of determination.
[e]FC-fractional contribution.
[f]Error of fit.

In current system realization, the time needed to collect the data of 150 cells ranges from 1.5 to 3 days. We are working to increase the throughput by at least one order of magnitude to enable faster data collection.

3.2 *Effect of Homotypic Cell-Cell Interactions on Cell Oxygen Consumption*

In the second part of this study, we focused on measurement of the effects of homotypic intercellular interactions on the OCRs of CP-A cells. We placed one, two, or three cells in each microwell using the custom cell manipulation platform (see Materials and Methods). All experiments were conducted using the same loading, incubation, and OCR measurement conditions as with single, non-interacting cells. Data obtained from the experiments with one cell per well were used as a reference for data from the experiments with two and three cells per well. Occasionally, the number of cells per well changed after the 16 to 24-h incubation period because of cell division and/or cell migration from the microwell. Therefore, prior to each experiment the number of cells in each well was counted using bright-field microscopy, and the data obtained from the wells were sorted accordingly. In most cases the cell morphology in wells containing more than one cell indicated that the cells were adhered to the bottom and walls of the microwell, and in some cases contacting one another [Fig. 2(a)].

Representative curves quantifying the kinetics of single and interacting cell respiration are depicted in Fig. 11. Each curve in the panels represents oxygen consumption kinetics of one [Fig. 11(a)], two [Fig. 11(b)], or three [Fig. 11(c)] cells. As expected, the OCR values increased with the number of cells per well. Nonetheless, some of the curves measured with one cell per well showed steeper slopes, i.e., faster respiration, compared with two cells per well [Fig. 11(a) cell 4, and curves in Fig. 11(b)]. It is unclear what could cause this significant increase in the OCR in an individual cell. It may be attributed to differences in the cell's phase in the cell cycle. It is possible, for example, that the cell 4 curve shown in Fig. 11(a) represents a cell in late G_2 or M phase, where the energy demand could be elevated because of imminent or ongoing cell division. In general, the data presented in Fig. 11 indicates that there are significant cell-to-cell variations in oxygen consumption rates. The slopes of the oxygen concentration time course differ up to ~6-fold with one cell per well, ~2-fold in wells containing two cells, and only 1.1 to 1.5-fold with three cells per well. This apparent decrease in OCR variability as the number of cells per well increases can be explained as the result of averaging the oxygen consumption behavior of two or three cells. This finding emphasizes an important feature of the approach: averaging for even as few as two cells can markedly alter measurement results.

To compare among experiments with different numbers of cells per microwell, we normalized the OCR values to the number of cells contained in a well (OCR_{norm}, Table 2) to obtain respiration rates in femtomoles per minute per cell. This allows for a direct comparison of oxygen consumption kinetics among the experiments. The results are summarized in Fig. 12. Comparison with OCR values obtained in microwells with single occupancy shows that, on average, the respiration rate per cell in microwells with three cells increases 4.46 times that of a cell in a microwell by itself. This finding indicates that the cellular respiration rate is strongly affected by the presence of neighboring cells of the same type. Moreover, the results imply that the level of increase in cellular respiration depends on the number of interacting cells. Compared to a lone cell, we do not observe an increase in the OCR when a single interacting neighbor is introduced, whereas a significant increase can be seen when three cells are allowed to interact in a microwell. The observed nonlinear dependence of oxygen consumption on the number of interacting cells implies the existence of complex cellular mechanisms which are capable of up or down-regulation of respiration rates in response to intercellular interactions. Interestingly, respiration measurements at bulk cell levels (~5.10^4 cells, 80% confluency, data not shown)

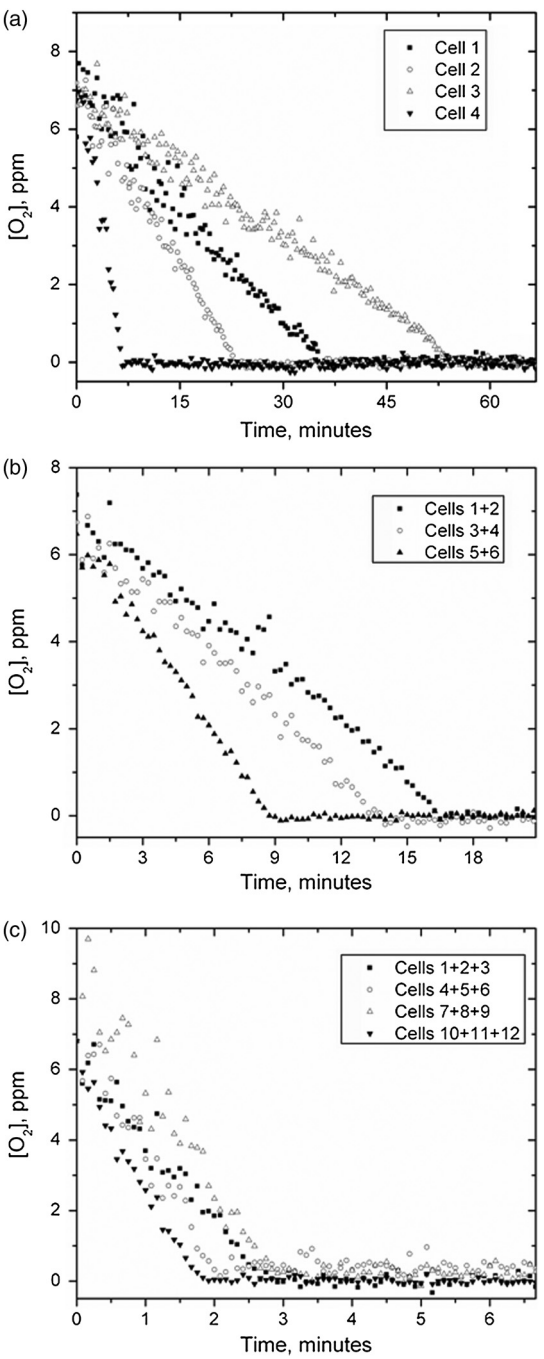

Fig. 11 Oxygen consumption curves measured with one (a), two (b), and three (c) CP-A cells per microwell. In general, because of averaging, the oxygen consumption kinetics show less well-to-well variation as the number of cells per well increases. *x*-axes are scaled differently in each plot.

Table 2 OCR measured with individual non-interacting and interacting CP-A cells.

Number of cells/well	OCR, fmol/ min	S.E.M.	OCR_{norm}, fmol/(min · cell)
1	3.14	0.10	3.14
1	1.28	0.01	1.28
1	0.87	0.01	0.87
1	0.532	0.003	0.532
2	3.23	0.03	1.61
2	2.13	0.02	1.06
2	1.78	0.02	0.89
3	14.9	0.4	4.96
3	14.2	0.6	4.73
3	10.2	0.4	5.10
3	12.9	0.7	6.45

with both CP-A and CP-C cells showed OCR values similar to the average OCR obtained in single-cell experiments. Although more detailed studies are needed to address this fact in more detail, the decrease in the average OCR in bulk samples may be a result of cell growth inhibition at high confluency levels. We are conducting more thorough studies, which focus on the effects of population size on cell respiration rate.

Although the data set is small, it is difficult to determine whether the observed increases in respiration rate were caused by direct cell-to-cell contacts, signaling mediated by soluble extracellular ligands, or both. Because some cells were in intimate contact with one another [Fig. 2(a)], all three alternatives are possible.

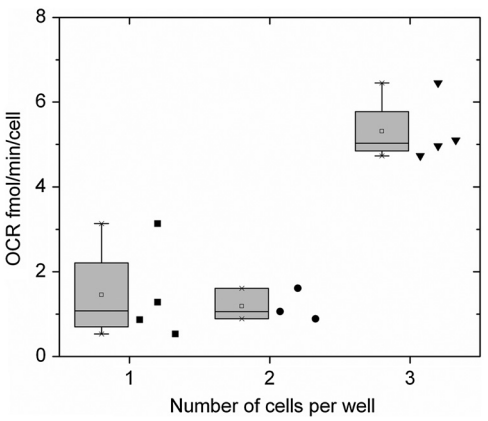

Fig. 12 OCRs of interacting cells. Descriptive statistics plot of data obtained with non-interacting, two interacting, and three interacting CP-A cells. Shows nonlinear increase in OCR with three interacting cells. The box chart shows following statistical values: Open square, mean; solid line, median; upper and lower box lines, the 75th and 25th percentiles, respectively; upper and lower whiskers, the 95th and 5th percentiles, respectively; and x, maximal and minimal values.

4 Conclusions and Future Outlook

In conclusion, these data demonstrate the capability of the experimental approach to perform robust oxygen consumption phenotype characterization at the single-cell level with individual, non-interacting or interacting cells with a moderate throughput of 50 to 100 cells/day. At 5 sec intervals, the data acquisition frequency was sufficient for fast respiring cells; this could be decreased further to 1 sec or less to account for even faster respiration rates, especially when multiple cells are placed in a microwell. The flexible design of the experimental platform permits loading of cells of several different types into microwells for heterotypic cellular interaction studies. In this study, we performed the measurements until oxygen concentration decreased to 0.1 ppm or lower, thereby exposing the cells to severe hypoxia or anoxia. However, by incorporating the ability to repeatedly raise and then reseal the lid array, the system design allows for measurements to be stopped and resumed with the same set of cells at any desired point in time. This enables, for example, introduction of chemical stimuli for drug dose-response studies, or for re-equilibration of the immediate cell environs with the surrounding medium. We were able to perform repeated oxygen consumption experiments with the same set of cells up to three times while completely depleting and re-equilibrating oxygen in the microwells (data not shown).

The platform design is flexible and adaptable, allowing for facile implementation of multisensor, multiparameter cellular phenotype characterization. The lid design can accommodate multiple spectrally-separable sensors, or be changed to accommodate multiple spatially isolated sensors. We are currently working on the development of a lid array that features multiple micropockets inside each microwell lid for deposition of different sensors to quantify multiple extracellular analytes in the same microwell. We are developing an ATP sensor system, and are in the process of optimizing custom optical sensors that can be embedded in polymer matrices pH, K^+, and temperature sensing.[36–39] In the near future we will combine a fully automated platform developed by our group for spectrally-resolved measurement of multiparameter sensor responses, combined with a microfluidics module for serial or parallel delivery of biochemical and environmental stimuli to cells confined in arrays of microwells. We will combine metabolic profile measurements with gene transcription level profiling at the single-cell level that will be applied after phenotype characterization to establish the relationships between expression levels of specific genes and cell phenotypes.[40] We will expand the scope of our studies to other cell types, to primary cells, and to the administration of a variety of stimuli using the automated multiparameter platform. We expect to increase the overall system throughput by using both modified cell-trapping approaches for highly parallel cell loading and polymer-mediated hermetic sealing techniques for increased cell array density.

Acknowledgments

Financial support for this work was provided by the Microscale Life Sciences Center, an NIH Center of Excellence in Genomic Sciences at Arizona State University [5P50 HG002360 and 3P50 HG002360-10S1 (ARRA) to D.R.M.]. We thank Brian Reid's group at the Fred Hutchinson Cancer Center for valuable discussions on cell physiology and for providing the CP-A and CP-C cell lines, and Courtney Hemphill and Patti Senechal-Willis for cell culture. We also thank Noel Fitzgerald, Michael

Konopka, Lloyd Burgess, Judy Anderson, Sei-Hum Jang, and Sarah McQuaide from the University of Washington for helpful discussions throughout these studies. We also thank Alan Brunner, Peter Kahn, and Peter Wiktor for the help with sensor deposition.

References

1. A. Raj and A. van Oudenaarden, "Nature, nurture, or chance: stochastic gene expression and its consequences," *Cell*, **135**(2), 216–226 (2008).
2. J. Rausenberger et al., "Signatures of gene expression noise in cellular systems," *Prog. Biophys. Mol. Biol.* **100**(1–3), 57–66 (2009).
3. B. Snijder et al., "Population context determines cell-to-cell variability in endocytosis and virus infection," *Nature* **461**(7263), 520–523 (2009).
4. R. Losick and C. Desplan, "Stochasticity and cell fate," *Science* **320**(5872), 65–68 (2008).
5. M. E. Lidstrom and D. R. Meldrum, "Life-on-a-chip," *Nat. Rev. Microbiol* **1**(2), 158–64 (2003).
6. T. Kalisky and S. R. Quake, "Single-cell genomics," *Nat Methods* **8**(4), 311–314 (2011).
7. N. Navin et al., "Tumour evolution inferred by single-cell sequencing," *Nature* **472**(7341), 90–94 (2011).
8. F. Tang et al., "mRNA-Seq whole-transcriptome analysis of a single cell," *Nat. Methods* **6**(5), 377–82 (2009).
9. Y. Taniguchi et al., "Quantifying E. coli proteome and transcriptome with single-molecule sensitivity in single cells," *Science* **329**(5991), 533–538 (2010).
10. J. Sun et al., "A microfluidic platform for systems pathology: multiparameter single-cell signaling measurements of clinical brain tumor specimens," *Cancer Res.* **70**(15), 6128–6138 (2010).
11. K. Smolková et al., "Mitochondrial bioenergetic adaptations of breast cancer cells to aglycemia and hypoxia," *J. Bioenerg. Biomembr.* **42**(1), 55–67 (2010).
12. M. Indelicato et al., "Role of hypoxia and autophagy in MDA-MB-231 invasiveness," *J. Cell. Physiol.* **223**(2), 359–368 (2010).
13. Y. Chen et al., "Oxygen consumption can regulate the growth of tumors, a new perspective on the Warburg effect," *PLoS One* **4**(9), e7033 (2009).
14. J. A. Bertout, S. A. Patel, and M. C. Simon, "The impact of O_2 availability on human cancer," *Nat. Rev. Cancer* **8**(12), 967–75 (2008).
15. M. Geissbuehler et al., "Triplet imaging of oxygen consumption during the contraction of a single smooth muscle cell (A7r5)," *Biophys. J.* **98**(2), 339–349 (2010).
16. S. Hatz, J. D. Lambert, and P. R. Ogilby, "Measuring the lifetime of singlet oxygen in a single cell: addressing the issue of cell viability," *Photochem. Photobiol. Sci.* **6**(10), 1106–1116 (2007).
17. I. Zebger et al., "Direct optical detection of singlet oxygen from a single cell," *Photochem. Photobiol.* **79**(4), 319–322 (2004).
18. M. R. Chatni and D. M. Porterfield, "Self-referencing optrode technology for non-invasive real-time measurement of biophysical flux and physiological sensing," *Analyst* **134**(11), 2224–2232 (2009).
19. D. M. Porterfield et al., "Characterization of oxygen and calcium fluxes from early mouse embryos and oocytes," *Biol. Bull.* **195**(2), 208–209 (1998).
20. R. Kashyap and M. Gratzl, "Adjusting the distance of electrochemical microsensors from secreting cell monolayers on the micrometer scale using impedance," *Anal. Chem.* **71**(14), 2814–2820 (1999).
21. R. T. Kurulugama et al., "Scanning electrochemical microscopy of model neurons: constant distance imaging," *Anal. Chem.* **77**(4), 1111–1117 (2005).
22. D. M. Osbourn, R. H. Sanger, and P. J. S. Smith, "Determination of single-cell oxygen consumption with impedance feedback for control of sample-probe separation," *Anal. Chem.* **77**(21), 6999–7004 (2005).
23. J. Dragavon et al., "A cellular isolation system for real-time single-cell oxygen consumption monitoring," *J. R. Soc. Interface* **5**(Suppl. 2), S151–S159 (2008).
24. J. R. Etzkorn et al., "Using micro-patterned sensors and cell self-assembly for measuring the oxygen consumption rate of single cells," *J. Micromech. Microeng.* **20**(9), 095017 (2010).
25. T. W. Molter et al., "A new approach for measuring single-cell oxygen consumption rates," *IEEE T. Autom. Sci. Eng.* **5**(1), 32–42 (2008).
26. T. W. Molter et al., "A microwell array device capable of measuring single-cell oxygen consumption rates," *Sensor. Actuator. B Chem.* **135**(2), 678–686 (2009).
27. E. J. Park et al., "Ratiometric fiber optic sensors for the detection of inter- and intra-cellular dissolved oxygen (Vol. 15, pp. 2913 2005)," *J. Mater. Chem.* **15**(31), 3246–3246 (2005).
28. S. M. Grist, L. Chrostowski, and K. C. Cheung, "Optical oxygen sensors for applications in microfluidic cell culture," *Sensors* **10**(10), 9286–9316 (2010).
29. H. X. Zhu et al., "Characterization of deep wet etching of fused silica glass for single cell and optical sensor deposition," *J. Micromech. Microeng.* **19**(6), 065013 (2009).
30. M. C. Palanca-Wessels et al., "Genetic analysis of long-term Barrett's esophagus epithelial cultures exhibiting cytogenetic and ploidy abnormalities," *Gastroenterology* **114**(2), 295–304 (1998).
31. Y. H. Anis, M. R. Holl, and D. R. Meldrum, "Automated selection and placement of single cells using vision-based feedback control," *IEEE T. Autom. Sci. Eng.* **7**(3), 598–606 (2010).
32. Y. Anis et al., "Diaphragm pico-liter pump for single-cell manipulation," *Biomed. Microdevices* **13**(4), 651–659 (2011).
33. E. Gnaiger, "Bioenergetics at low oxygen: dependence of respiration and phosphorylation on oxygen and adenosine diphosphate supply," *Resp. Physiol.* **128**(3), 277–297 (2001).
34. A. Garedew, U. Kammerer, and D. Singer, "Respiratory response of malignant and placental cells to changes in oxygen concentration," *Resp. Physiol. Neurobiol.* **165**(2–3), 154–160 (2009).
35. E. Hutter et al., "Biphasic oxygen kinetics of cellular respiration and linear oxygen dependence of antimycin A inhibited oxygen consumption," *Mol. Biol. Reports* **29**(1–2), 83–87 (2002).
36. Y. Q. Tian et al., "Dually fluorescent sensing of pH and dissolved oxygen using a membrane made from polymerizable sensing monomers," *Sensor. Actuator. B Chem.* **147**(2), 714–722 (2010).
37. Y. Q. Tian et al., "A series of naphthalimide derivatives as intra and extracellular pH sensors," *Biomaterials* **31**(29), 7411–7422 (2010).
38. X. Zhou et al., "Triazacryptand-based fluorescent sensors for extracellular and intracellular K(+) sensing," *Biomaterials* **32**(33), 8574–83 (2011).
39. X. Zhou et al., "Platinum (II) porphyrin-containing thermoresponsive poly(N-isopropylacrylamide) copolymer as fluorescence dual oxygen and temperature sensor," *Sensor. Actuator. B Chem.* **159**(1), 135–141 (2011).
40. J. Zeng et al., "Quantitative single-cell gene expression measurements of multiple genes in response to hypoxia treatment," *Anal. Bioanal. Chem.*, **401**(1), 3–13 (2011).